

Bandgap Engineering of Organic Semiconductors for Highly Efficient Photocatalytic Water Splitting

Yiou Wang, Fabrizio Silveri, Mustafa K. Bayazit, Qiushi Ruan, Yaomin Li, Jijia Xie, C. Richard A. Catlow,* and Junwang Tang*

The bandgap engineering of semiconductors, in particular low-cost organic/polymeric photocatalysts could directly influence their behavior in visible photon harvesting. However, an effective and rational pathway to stepwise change of the bandgap of an organic/polymeric photocatalyst is still very challenging. An efficient strategy is demonstrated to tailor the bandgap from 2.7 eV to 1.9 eV of organic photocatalysts by carefully manipulating the linker/terminal atoms in the chains via innovatively designed polymerization. These polymers work in a stable and efficient manner for both H₂ and O₂ evolution at ambient conditions (420 nm < λ < 710 nm), exhibiting up to 18 times higher hydrogen evolution rate (HER) than a reference photocatalyst g-C₃N₄ and leading to high apparent quantum yields (AQYs) of 8.6%/2.5% at 420/500 nm, respectively. For the oxygen evolution rate (OER), the optimal polymer shows 19 times higher activity compared to g-C₃N₄ with excellent AQYs of 4.3%/1.0% at 420/500 nm. Both theoretical modeling and spectroscopic results indicate that such remarkable enhancement is due to the increased light harvesting and improved charge separation. This strategy thus paves a novel avenue to fabricate highly efficient organic/polymeric photocatalysts with precisely tunable operation windows and enhanced charge separation.


1. Introduction

Photocatalytic water splitting has attracted substantial attention over the past 40 years as a promising approach to mitigate key energy and environmental issues.^[1] As the photocatalytic

Y. Wang, Dr. M. K. Bayazit, Q. Ruan, Y. Li, J. Xie, Prof. J. Tang
Solar Energy and Advanced Materials Group
Department of Chemical Engineering
UCL

Torrington Place, London WC1E 7JE, UK
E-mail: junwang.tang@ucl.ac.uk

F. Silveri, Prof. C. R. A. Catlow
School of Chemistry
University of Cardiff
Park Place, Cardiff CF10 3AT, UK
E-mail: catlowr@cardiff.ac.uk

 The ORCID identification number(s) for the author(s) of this article can be found under <https://doi.org/10.1002/aenm.201801084>.

© 2018 The Authors. Published by WILEY-VCH Verlag GmbH & Co. KGaA, Weinheim. This is an open access article under the terms of the Creative Commons Attribution License, which permits use, distribution and reproduction in any medium, provided the original work is properly cited.

The copyright line for this article was changed on August 27, 2018 after original online publication.

DOI: 10.1002/aenm.201801084

activity is highly dependent on the electronic structure of the photocatalyst, it is crucial to adjust the bandgap in order to utilize the highest possible proportion of visible photons and achieve the target of 10% solar to fuel conversion efficiency.^[2] Moreover, bandgap tunable semiconductors are especially useful in the construction of a Z-scheme for water splitting, which is considered to be a more promising approach to solar H₂ production than the single photocatalyst-based water splitting system.^[3–8] A Z-Scheme requires an appropriate match of redox potentials between two photocatalysts and two mediators. So far, the strategies that have been successfully applied to change the bandgaps and band positions of photocatalysts include heteroatom doping and the use of junctions between materials. For instance, the doping of cations (e.g., Rh) into SrTiO₃ introduced new energy levels and narrowed its wide bandgap (3.1 eV) to the visible light region (2.4 eV).^[9] Another well-known exemplar is the solid solution of GaN: ZnO (2.5 eV), which forms a visible light responsive bandgap from two UV-responsive semiconductors (3.4 and 3.2 eV).^[10]

Compared with the progress in bandgap engineering of inorganic photocatalysts, there have been limited reports of the emerging organic photocatalysts (e.g., heptazine-based polymers and covalent organic frameworks), although they are known for their suitable band positions for water splitting, low-cost, chemical stability, and good tunability of their framework and electronic structures.^[11–17] Currently, the majority of organic/polymeric photocatalysts still suffer from an intrinsic wide bandgap (e.g., \approx 2.7 eV for g-C₃N₄) and only responds to a limited region of the solar spectrum (<460 nm), not matching with the strongest portion of 450–700 nm in sunlight (2.7–1.8 eV photons).^[18,19] Although approaches such as element doping, copolymerization, and introduction of defects have attempted to narrow the bandgap to \approx 2.0 eV, the resultant operation window is either far from the target region or the apparent quantum yield (AQY) is still moderate, probably due to defect-induced recombination centers.^[20–22] The lack of facile bandgap engineering methods has inhibited the application of organic/polymeric photocatalysts to potential applications including the construction of Z-scheme water splitting systems. Therefore, an effective and rational polymerization strategy to stepwise engineer precisely the electronic structure of polymers is a real need scientifically and technically.

Taking graphitic carbon nitride (g-C₃N₄ or GCN), the most widely reported heptazine-based polymers, as an instance, the conduction band (CB) is considered to consist of conjugated C and N 2p orbitals in the heptazine while the VB is mostly composed of the 2p orbitals of edge N atoms, resulting in a π - π^* excitation bandgap of over 2.7 eV.^[23,24] A disordered framework could allow n- π^* excitation of the lone pair electrons on edge N atoms that is forbidden in a planar structure, which would result in a photon energy that is smaller than 2.5 eV and was reported to aid the visible light absorption.^[25,26] Very recently, we have theoretically and experimentally proved that the oxygen and nitrogen linker-controlled heptazine-based chains strongly influence the polymer's electronic structure.^[27] The band positions of O-linked chains are relatively more positive than those of N-linked chains, hence the hybrid polymer consists of a lower CB contributed by the introduced O-linked chains and a VB contributed by N-linked chains, resulting in a narrowed bandgap. More importantly, the electron acceptor-donor nature between O-chains and N-chains promotes the physical charge separation for enhanced efficiency.^[28] Also, the selective doping into the linker position instead of heptazine units in the polymer maintains an integrated conjugated framework and avoids additional defect-based recombination centers. However, this modified polymer is only active for H₂ production with no activity for water oxidation under visible light irradiation.

In this study, based on the previous work, we developed a new approach to control precisely the bandgap of organic photocatalysts, resulting into stepwise bandgap changes from 2.7 to 1.9 eV, by carefully tailoring the linker and terminal atoms among donor-acceptor domains. This fine control of band positions has been achieved by adding different amounts of formic acid as an important precursor and an innovative stoichiometry-tuned polymerization, which provides an effective way to synthesize a series of polymer photocatalysts with controlled electronic structures. Furthermore, this approach allows us to observe the correlation between the band positions and photocatalytic activities of polymer semiconductors. The resultant polymers work in a stable and efficient manner for H₂ and more importantly O₂ evolution at ambient conditions under visible light irradiation (420 nm < λ < 710 nm), representing not only up to 18 times higher hydrogen evolution rate (HER) than the widely reported pristine g-C₃N₄, but also nearly 20 times higher oxygen evolution rate (OER) activity. More importantly these activities are well correlated with the band position changes of the polymers.

2. Results and Discussion

2.1. The Design of Polymerization Pathway

In order to engineer the bandgap of the heptazine-based polymers, the novel polymerization pathway was carefully designed and controlled as shown in Scheme S1 (Supporting Information). As reported before, the band position shift originates from the existence of O-linked chains connected to N-linked domains, which have lower (more positively orientated) CB with an electron acceptor nature as illustrated in our recent

study.^[27,28] The total electronic structure of such hybrid polymers consists of CB contributed by O-chains and VB contributed by N-chains, resulting in a narrow bandgap. Therefore, it is crucial to control the O-terminated heptazine monomers during the polymerization to tailor the bandgap. Different from DCDA precursor that undergoes a widely accepted melamine-melam-melon-g-C₃N₄ pathway (Scheme S1, Supporting Information, the upper),^[11] the formic acid treated precursor involves additional intermediates including hydroxyl- and amine-terminated heptazine (Scheme S1, Supporting Information, the lower) as monomers,^[29,30] resulting in O-linked heptazine in the following process. Also, some unreacted DCDA molecules will form ordinary N-linked heptazine, which polymerize together with O-linked ones. By stoichiometrically controlling the amount of formic acid in the pretreatment, the ratio between O-linked and N-linked chains and the extent of CB shift in the final produced polymers can be stepwise controlled; hence the properties including the electronic structure of polymers can be tuned reproducibly and reliably.

Such a proposed polymerization routine has been examined in detail by characterization of intermediates. The structural differences are shown in Carbon-13 solid-state nuclear magnetic resonance (¹³C ssNMR) of intermediates obtained at different temperatures during the polymerization of acid-treated precursors (Figure S1a, Supporting Information). For example, at 130 °C, the two peaks at 120 (cyano group) and 164 ppm are from the residual DCDA while those at 170 and 158 ppm are related to carbon atoms in O containing intermediates.^[31–33] No polymerization was expected at 130 °C, thus NMR spectra show the mixture of unreacted and formic acid treated DCDA. This is further confirmed by FTIR, which shows the features of both DCDA and cyanuric acid. As the temperature rises from 130 °C to 350 °C, the precursor transforms from a triazine-like structure to a heptazine-like structure because the 158 ppm peak submerges in NMR at 350 °C, indicating the inner circle carbon formation in heptazine^[34] and the heptazine C–N vibration peaks appear at 1350–1200 cm⁻¹ in FT-IR.^[18,35] In the final product formed at 450–550 °C, the oxygen characters are less obvious due to a low concentration and an overlap with other species but the broader peaks due to a disordered structure are similar to the previously reported.^[27]

Thermogravimetric analysis (TGA) and differential scanning calorimetry (DSC) analysis support the proposed pathway. With the DCDA representing the same as that reported during thermal condensation,^[11] the acid-treated precursor has two melting points at 130 °C and 190 °C corresponding to the mixture compositions in the acid-treated precursor. The FAT intermediates went through triazine \approx 236 °C and formed heptazine after 300 °C.^[29] As observed, the polymerization behavior of FAT sample is similar to g-C₃N₄ but at a lower temperature, probably owing to the precyclization at a lower temperature (Scheme S1, Supporting Information, lower) which aids the next step of the polymerization.^[29] Notably, the color of the FAT intermediate starts changing from white to brown during polymerization \approx 250 °C while DCDA remains white until the final step to yellow after 450 °C. Such an obvious color change of FAT intermediates indicates that the bandgap shift due to the oxygen-containing groups appears at relatively lower temperatures in the polymerization process.

Table 1. Summary of the properties of FAT samples measured at atmospheric pressure.

Samples	Composition	N content [%]	O content [%]	Surface area [m ² g ⁻¹]	Bandgap [eV]	HER [μmol g ⁻¹ h ⁻¹]
FAT-0	C ₃ N _{4.51} H _{1.6} O _{0.07}	49.1	0.76	5.5	2.74	44
FAT-0.1	C ₃ N _{4.50} H _{1.7} O _{0.07}	49	0.76	5.6	2.72	103
FAT-0.2	C ₃ N _{4.49} H _{1.6} O _{0.07}	49	0.76	6.7	2.69	114
FAT-0.5	C ₃ N _{4.48} H _{1.6} O _{0.07}	49	0.77	6.9	2.66	192
FAT-0.8	C ₃ N _{4.44} H _{1.7} O _{0.09}	48.1	0.98	9.9	2.06	456
FAT-1.0	C ₃ N _{4.43} H _{1.8} O _{0.15}	47.7	1.62	12.1	1.92	772
FAT-1.5	C ₃ N _{4.40} H _{2.0} O _{0.25}	45.5	2.67	16.4	2.01	656
FAT-2.0	C ₃ N _{4.33} H _{2.0} O _{0.26}	45.2	2.71	40.0	2.05	556

2.2. Characterizations of Novel Organic Semiconductors

These bandgap tunable polymers are synthesized at 550 °C for 4 h and the final products are noted as FAT-X with X representing the stoichiometry ratio of formic acid to DCDA in the precursors. FAT-0 is the reference DCDA-derived g-C₃N₄. The properties of the synthesized polymers with different amounts of formic acid in precursors were investigated via extensive and thorough characterizations. From elemental analysis (EA), the bulk atomic stoichiometry of eight FAT samples was found to be: C₃N_{4.51}H_{1.6}O_{0.07} (FAT-0), C₃N_{4.50}H_{1.7}O_{0.07} (FAT-0.1), C₃N_{4.49}H_{1.6}O_{0.07} (FAT-0.2), C₃N_{4.48}H_{1.6}O_{0.07} (FAT-0.5), C₃N_{4.44}H_{1.7}O_{0.09} (FAT-0.8), C₃N_{4.43}H_{1.8}O_{0.15} (FAT-1.0), C₃N_{4.40}H_{2.0}O_{0.25} (FAT-1.5) and C₃N_{4.33}H_{2.0}O_{0.26} (FAT-2.0) (Table 1). As the amount of formic acid increases in the precursors, the polymers show a decreasing amount of nitrogen

with increasing oxygen, indicating more O species in the polymers' bulk structure. Unlike some recently reported copolymerization polymers with slightly different features from g-C₃N₄, the FAT samples exhibit distinct and stepwise changes.

To obtain the crystallinity information of FAT polymers, powder X-ray diffraction (PXRD) patterns of the samples were measured (Figure 1a). At first glance, the patterns of the FAT samples are similar to FAT-0 (g-C₃N₄) in shape, which has two peaks locating at 13.0° and 27.4° assigned to the (100) and (002) planes, respectively, corresponding to intralayer packing size of 6.82 Å and an interlayer distance of 3.26 Å.^[22] A close examination shows that the (100) peak of the other FAT samples becomes weaker and slightly right shifts to 13.4°, indicating a reduced crystallinity and a closer crystalline distance of 6.67 Å probably due to small polymer size and the shorter bond lengths in the presence of oxygen.^[33] It is more evident

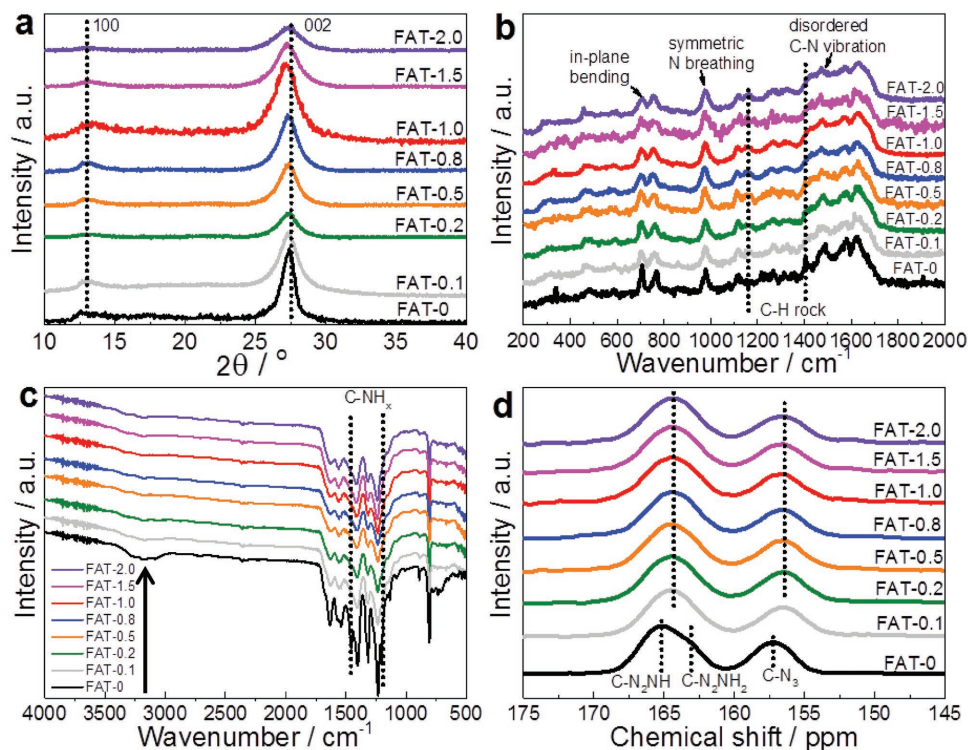


Figure 1. a) X-ray diffraction patterns, b) Raman spectra, c) FT-IR spectra, d) ¹³C solid-state nuclear magnetic resonance (ssNMR) spectra of different FAT samples.

that (002) peaks shift left, suggesting an enlarged layer-to-layer distance up to 3.30 Å due to a variation in structure, such as distortions in the FAT samples or the oxygen species between layers.^[27] The width of the (002) peak becomes broadened as the amount of formic acid increases, which also suggests that the crystalline size of the polymers is smaller. The shifts of peak positions are consistent with the change in the formic acid equivalent, suggesting the higher amount of O-containing groups, the larger shift of peak positions. Both the highest peak density and largest shift distance is found on the sample FAT-1.0. Further increasing formic acid concentration causes the peak shift to decrease. One can see formic acid in the precursor first results in a decline of polymerization degree (Figure 1a, FAT-0.1). As the amount further increases, relatively well-crystallized product gradually forms because the XRD patterns become sharper from FAT-0.2 to FAT-1.0. After that, extra formic acid in the precursor leads to poor polymerization again. Therefore, FAT-1.0 and FAT-0 (g-C₃N₄) could be two relatively highly crystallized polymers.

Raman spectroscopy was used to detect the backbone of the FAT polymers (Figure 1b). From the spectra, the heptazine-based structure could be confirmed as most of these characteristic peaks appear at the same positions. The peaks in the 1200–1700, 980, and 690 cm⁻¹ regions represent the disordered graphitic carbon–nitrogen vibrations, the symmetric N-breathing mode of heptazine and the in-plane bending, respectively.^[36,37] Notably, the peak at 1406 cm⁻¹ in FAT-0 (g-C₃N₄) becomes negligible while the one at 1170 cm⁻¹ emerges as the amount of formic acid goes up. These two modes are both in-plane C–H rock and semicircle stretching but in different directions.^[37] Such a change toward disordered structure could be assigned to the oxygen-linked chains. Similar to the intensity trend of XRD patterns, the intensity of signals from FAT-0 to FAT-1.0 and to FAT-2.0 shows a volcano curve. As discussed above, this results from the differences in the degree of crystallinity induced by oxygen amount.

In order to confirm the difference of structure, FT-IR spectra of FAT polymers were also compared. Generally, FAT samples have similar but broadened and less sharp peaks, owing to the incorporation of oxygen species into the structure (Figure 1c).^[27] As no peaks show up in around 2200 and 1700 cm⁻¹ region, the existence of C=O from formic acid and cyano groups from DCDA has been ruled out, indicating these precursors were converted during polymerization.^[38] As the amount of formic acid increases, peaks of all other FAT samples at 1207 and 1455 cm⁻¹ (indicated by dotted line in Figure 1c) related to C–NH_x are gradually getting weaker than those of FAT-0 (g-C₃N₄) (Figure S2a, Supporting Information),^[35] while identical peaks of NH_x ≈ 3000–3300 cm⁻¹ in other FAT samples decline and an additional peak assigned to –OH emerges at 3340 cm⁻¹ (Figure S2b, Supporting Information), altogether verifying the decline of NH_x groups and the formation of –OH species.^[18,39]

¹³C ssNMR was used to illustrate such a structural change in detail (Figure 1d). The characteristic peaks of FAT-0 (g-C₃N₄) around 166, 163, and 157 ppm are assigned to external circle carbons (C_e: CN₂NH and CN₂NH₂) and inner circle carbons (C_i: CN₃), respectively (Figure 1d and Figure S3, Supporting Information).^[31,34] The overall NMR chemical shift suggests that FAT polymers consist of a mixture of N-linked heptazine

(melem) and O-linked heptazine. The observed right-shifted peaks in FAT samples by about 1 ppm with weakening NH_x related signals result from the substitution of N linkers by oxygen bridges and terminals, which also matches the trend obtained from the NMR prediction software (Figure S3, Supporting Information).^[40–42]

X-ray photoelectron spectroscopy (XPS) was also undertaken to investigate the chemical state in these materials (FAT-1.0 as one example was shown in Figure S4, Supporting Information). According to the depth profile of O 1s XPS spectra, the spectrum peak shifts from 531.8 to 533.2 eV as the etching goes deeper from 0 to 130 nm (Figure S4a, Supporting Information). As observed, there are four types of O species on the surface of FAT-1.0, which are surface oxides C=O (530 eV),^[43] C–OH bond (531.5 eV),^[44] adsorbed water (532.5 eV),^[45,46] and C–O–C bond (533.2 eV) (Figure S4b, Supporting Information).^[47] After etching to 130 nm, only two obvious peaks of C–OH and C–O–C are detected (Figure S4c, Supporting Information), confirming the existence of oxygen linkers and OH terminals in the bulk materials. Therefore, the peak shift during the etching is assigned to the decline of surface species (C=O, some C–O and water). According to C1s XPS spectra, the ratio of compositions of C–O to C–N (C–O/C–N) keeps increasing with an increasing amount of formic acid (Table S1, Figure S5, Supporting Information), indicating a decreased amount of N and an increased amount of O species in these polymers.^[27] These results confirm oxygen linkers (and OH terminals) in the structure, which should affect the properties of FAT polymers.

Comparing the scanning electron microscopy (SEM) images between FAT-0 (g-C₃N₄) and FAT-1.0 (Figure 2a), it is observed that the former has a stacking layered structure while the latter shows a ribbon-like structure.^[48] This is consistent with the less crystallized structure inferred from XRD patterns and Raman spectra. The hierarchical network/ribbon like structure of FAT-1.0 samples is also different from the previously reported polymer due to a new synthetic protocol.^[27] The distortions in FAT samples allow more n–π* transitions from the edge N atoms to the CB, which might also aid the visible photon absorption.^[24] The fiber-like structure of FAT-1.0, instead of the packing plane-like FAT-0, should possess a higher surface area and a better contact with water.^[49]

In order to investigate the influence of surface area, Brunauer–Emmett–Teller (BET) surface area measurements were carried out (Table 1). Consistent with the differences in SEM images, the surface area continuously increases from 5.5 to 40 m²g⁻¹ from FAT-0 to FAT-2.0 samples, probably due to the releasing of oxygen-containing species during the polymerization of oxygen precursors, similar to the thermal exfoliation of graphene oxide.^[50–52] Therefore, the characterizations of PXRD, Raman, SEM, FT-IR NMR, and XPS have confirmed the proposed framework of FAT polymers composed of distorted oxygen and nitrogen colinked heptazine units.

An apparent visual difference among FAT-0 (g-C₃N₄) to FAT-1.0 samples is the color changes step-by-step from pale yellow to dark brown (Figure 2b and photos in Figure S6a, Supporting Information). As mentioned above, the bandgap engineering of photocatalysts could directly influence the harvest of visible photons, the driving force as well as the charge transfer behavior. The bandgaps^[11] of FAT samples were determined

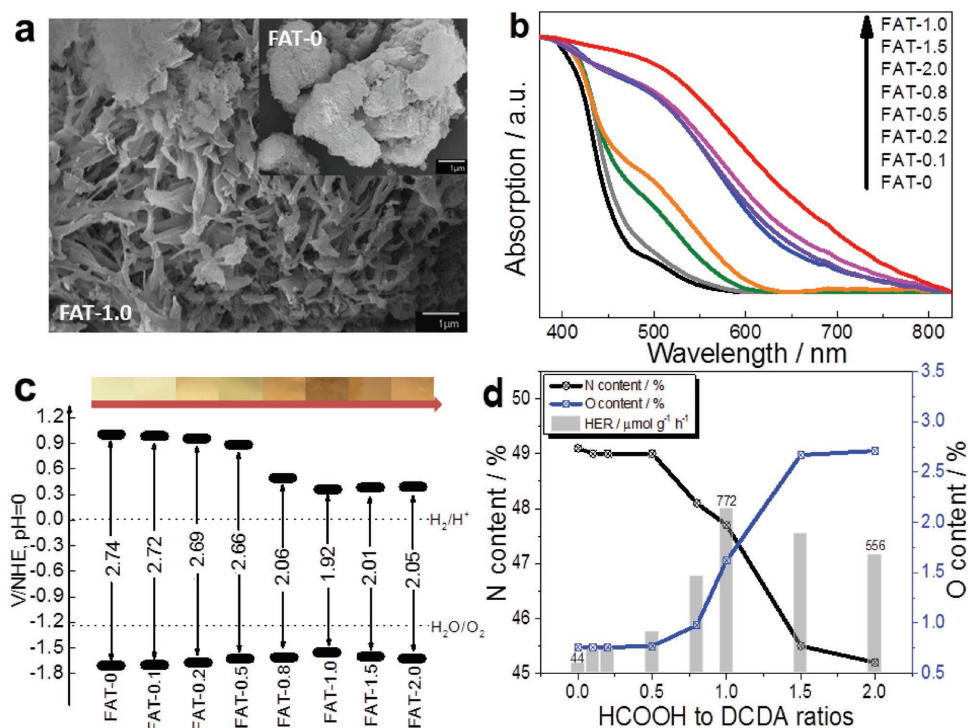


Figure 2. a) SEM images of the FAT-1.0 and FAT-0 ($g\text{-C}_3\text{N}_4$) (inset), b) UV-vis spectra, c) band alignment (V/NHE, pH 0) (top: color photos) of FAT samples and d) N contents, O contents, and hydrogen evolution rates (HER) under visible light irradiation ($420\text{ nm} < \lambda < 710\text{ nm}$) of FAT samples.

as a Tauc plot calculated from UV-vis spectra (Figure 2b and Figure S6a, Supporting Information). Such a stepwise bandgap change from 2.7 eV (FAT-0) to final 1.9 eV (FAT-1.0) is clearly due to increasing oxygen amount in the polymers (Table 1, Figure 2c). A gap between the absorption curves of FAT-0.5 and FAT-0.8 divides the samples into two groups. Further increasing the amount of acid in the precursor does not result in a narrower bandgap. On the contrary, the bandgaps of FAT-1.5 and 2.0 are slightly wider than FAT-1.0, which might be due to the excess amount of introduced O atoms.

To investigate the band positions, XPS valence band spectra (Figure S6b, Supporting Information), Mott-Schottky plots (Figure S6c,d, Supporting Information) along with the Tauc plot (Figure S6a, Supporting Information) were used to determine the band alignment as shown in Figure 2c and Table S2 (Supporting Information). With the VB of FAT samples slightly changing, the narrow bandgaps of FAT samples mainly result from the down shift of CB. From FAT-0 to FAT-0.5, the CB position only moves moderately. From FAT-0.8 to FAT-2.0, the CB apparently moves downward (more positive) but is still sufficient to drive proton reduction, attributed to the cooperation of O-linked chains. While O-linked chains create defects and distortions in the low concentration polymers (FAT-0 to FAT-0.5), which allows $n\text{-}\pi^*$ transition, the CB shift is more distinct in samples with more O-linked chains (FAT-0.8 to FAT-2.0).

2.3. The Evaluation of Photocatalytic Performance

After successful synthesis of bandgap tunable FAT polymers and illustration of their framework and electronic structures, the

photocatalytic capabilities of FAT samples were fully evaluated. The H_2 evolution rates (HERs) were measured in the presence of 3 wt% Pt co-catalyst (Figure S6e, Supporting Information) and 10% TEOA solution under 1 bar pressure and the visible irradiation ($420\text{ nm} < \lambda < 710\text{ nm}$) of 300 W light source (Newport-66485-300XF-R1, $\approx 100\text{ mW cm}^{-2}$). No activity was detected in the absence of light, photocatalysts, or electron donor. As the amount of nitrogen decrease and that of oxygen increases due to an increased amount of formic acid in the precursors, the HERs show a volcano-like trend peaking at FAT-1.0 (Figure 2d). From FAT-0 ($g\text{-C}_3\text{N}_4$) to FAT-1.0, the HER gains an 18-fold increase from 44 to $772\text{ }\mu\text{mol g}^{-1}\text{ h}^{-1}$ and then decreases from FAT-1.0 to FAT-2.0. Such dramatically enhanced performance of FAT-1.0 is believed to be related to the narrowest bandgap, which utilizes maximum visible photons and the HER trend supports such relationship (Figure 2c,d). A further excess amount of formic acid probably shields the amine groups in precursors too much and results in the low degree of polymerization (e.g., FAT-1.5 and FAT-2.0 samples), thus slightly decreasing the activity due to defects as recombination centers.^[18] The HER of FAT-0 to FAT-0.5 only increases moderately but exhibits a sharper increment after FAT-0.8, indicating a good correlation between the bandgap and photocatalytic activity.^[24] The synthesized FAT polymers also maintain a highly reproducible activity during the 30 h run (or seven cycles, Figure 3a), proving the incorporation of O at the linker/terminal positions instead of into heptazine units does not affect the stability. The apparent quantum yield (AQY) measured on the optimum FAT-1.0 sample was determined to be 8.6% at 420 nm and 2.5% at 500 nm and it also shows activity at 600 and 700 nm, following the same profile of the UV-vis absorption spectrum and indicating a light driven reaction (Figure 3b).

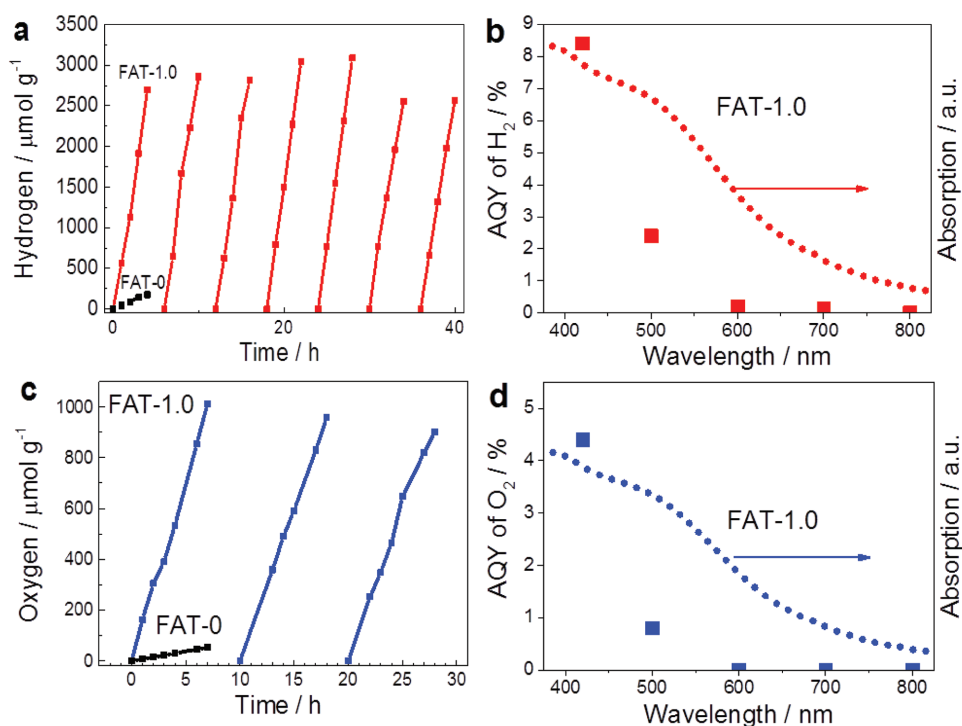


Figure 3. a) Hydrogen evolution rates (HER) stability tests ($420 \text{ nm} < \lambda < 710 \text{ nm}$) for 30 h and b) apparent quantum yield (AQY) measurements of H_2 at different wavelengths on Pt-FAT-1.0 samples in presence of 10% TEOA as a hole scavenger. c) Oxygen evolution rates (OER) stability tests ($420 \text{ nm} < \lambda < 710 \text{ nm}$) for 25 h and d) apparent quantum yield (AQY) measurements of O_2 at different wavelengths on PtO_x -FAT-1.0 samples in presence of $5 \times 10^{-3} \text{ M NaIO}_3$ as an electron scavenger.

As FAT-0 does not work beyond 460 nm, the superior activity of FAT-1.0 in the whole visible region is again attributed to the narrowed bandgap.

As N-linked heptazine polymers (FAT-0 or $g\text{-C}_3\text{N}_4$) have been also reported to achieve water oxidation although its activity is very moderate,^[11] we also examined whether the highly active FAT samples would show an enhanced performance of the water oxidation reaction. Surprisingly, the PtO_x -FAT-1.0 exhibited OER of $145 \mu\text{mol g}^{-1} \text{ h}^{-1}$, which is 19 times higher than that of PtO_x -FAT-0 ($7.5 \mu\text{mol g}^{-1} \text{ h}^{-1}$) (Figure 3c) under $5 \times 10^{-3} \text{ M IO}_3^-$ aqueous conditions (Figure 3c and Figure S6f, Supporting Information) under ambient conditions and visible light irradiation ($420 \text{ nm} < \lambda < 710 \text{ nm}$). The electron acceptor used here is IO_3^- because the commonly used Ag^+ would shield the surface of a photocatalyst hence its activity cannot be continuously tested.^[53] In Figure 3d, the long period stability also validates that the oxygen is produced from water. Moreover, the oxygen content contained in 20 mg FAT-1.0 is 14.4 μmol according to the elemental analysis (Table 1), while the total amount of oxygen produced during the three cycles reached 57.5 μmol (Figure 3d), which is much more than the oxygen amount contained in materials, thus clearly demonstrating that the oxygen production is derived from water oxidation.^[11] FAT-1.0 also displays a high apparent quantum yield (AQY) of 4.3% and nearly 1.0% at 420 and 500 nm for water oxidation (Figure 3d), respectively, surpassing the previous OER on $g\text{-C}_3\text{N}_4$ (1.1% and 0 at 420 and 500 nm in $10 \times 10^{-3} \text{ M Ag}^+$).^[53] The superior performance for both H_2

evolution and O_2 evolution on the bandgap tunable FAT samples makes them promising candidates for the construction of Z-scheme water splitting.

2.4. The Origin of Superior Performance

To interpret the trend of enhanced activity as well as the structural change of FAT polymers, we refer to both experimental and theoretical approaches. Photoelectrochemical properties were investigated to compare the significant enhancement in photocatalytic performance on the FAT samples. As shown in Figure 4a, the photocurrent performance on the FAT-1.0 sample and FAT-0 shows a nearly 26 fold difference, consistent with the measured HER.^[54] Photoluminescence (PL) measurements were used to compare the charge separation capability on the FAT samples using a UV laser (325 nm, Figure 4b). The peak near 420 nm is assigned to emissions from band edges involving π -conjugated states. While the larger portion of recombination signals are those $\approx 500\text{--}600 \text{ nm}$ corresponding to the intra states including $n\text{-}\pi^*$ transition and defect-based states.^[55,56] From FAT-0 to FAT-2.0, PL peaks gradually decreases and the peak intensity trend reversely agrees with the HER on FAT polymers, indicating that a stepwise enhanced charge separation was obtained on the doped samples. The optimum sample FAT-1.0 shows about two magnitudes lower intensity than FAT-0. Moreover, with the bandedge peaks anchoring at 420 nm, the intra state peaks move from

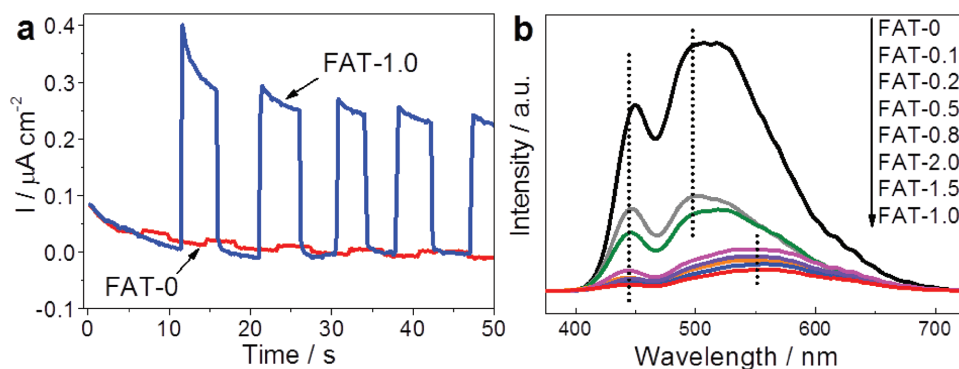


Figure 4. a) Periodic on/off photocurrent response of FAT-0 and FAT-1.0 electrodes in 0.1 M Na_2SO_4 with 0.6 V bias versus Ag/AgCl. b) Photoluminescence spectra (excited by 325 nm laser) of FAT samples.

500 to 600 nm as the amount of formic acid goes up, verifying the process of the band structure narrowing due to additional oxygen-linked chains.^[55] Therefore, less radiative electron-hole recombination and extensive light harvest ability due to narrow band states of FAT samples would promote their photoactivity. Other factors might influence the performance to some extent, such as surface area. However, FAT-1.0 ($12.1 \text{ m}^2 \text{ g}^{-1}$) instead of the samples with the larger surface area (FAT-1.5, $16.4 \text{ m}^2 \text{ g}^{-1}$ and FAT-2.0, $40.0 \text{ m}^2 \text{ g}^{-1}$), achieves the highest HER, so the enhancement in activity cannot be directly attributed to surface area.^[18] It should be noted that the PL signals slightly increase again in samples from FAT-1.0 to FAT-2.0. Similarly, the trend of structural characterizations and gas evolution measurements also peak at FAT-1.0 while more oxygen content does not contribute further to the enhancement.

Further explanation for this phenomenon comes from the results of computational work conducted on the system, which show a direct relationship between the incorporation of the oxygen within the framework and the electronic structure and hence the predicted performance of polymers. As previously showed, the oxygen content is incorporated in the framework outside the heptazine (tri-s-triazine) rings, replacing an $-\text{NH}-$ group either by linking two rings or by terminating a chain (Figure S7, Table S3, Supporting Information). The models, shown in detail in Figure S7 (Supporting Information), are composed of four linear chains organized in two layers, with a total of eight tris-triazine rings. In $\text{g-C}_3\text{N}_4$, this configuration would correspond to 8 $-\text{NH}_2$ terminal groups and 8 $-\text{NH}-$ linker groups in a unit cell. To model the high oxygen content FAT polymers (FAT-0.8 and over), 4 of those groups are substituted with either $-\text{OH}$ terminals or $-\text{O}-$ linkers. This set up allowed us to investigate the different oxygen configurations that can be found locally within the polymer, which will be proved to have a major effect on the performance of the material.

The density functional theory (DFT) calculations show how the substitution of $-\text{NH}-$ groups is favorable, as the formation energy goes from $+13.05$ to $-10.33 \text{ kJ mol}^{-1}$ for the modeled O-linked polymers. The stability increases even further when oxygen is incorporated as $-\text{OH}$ linkers (Table S4, Supporting Information), but the electronic effect of the two substitutions appears to be similar. Density of state (DOS) calculations

have also been performed. The calculations present a smaller bandgap than experiment for $\text{g-C}_3\text{N}_4$ (see the Computational Methodology section for more detail), although this underestimation of the bandgap is expected. Interestingly, the calculated gaps for the FAT samples compare reasonably with experiment but in view of the known inadequacy of Perdew–Burke–Ernzerhof (PBE)–DFT in calculating bandgaps, no further use of calculated bandgaps is made in our analysis.

However, a subtle difference between the oxygen arrangements seems to drive the electronic structure, as shown by the decomposed charge density of the valence and conduction bands. According to the EA (Table 1) of FAT samples, the oxygen content increases and the nitrogen content declines as more formic acid is added in the precursor, corresponding to the gradual substitution of $-\text{NH}-$ groups with oxygen in the polymer. The coexistence of N-containing chains and O-containing chains in the FAT polymers can drastically improve the charge separation due to the N-chains' electron donor nature and O-chains' electron acceptor nature: when the oxygen is distributed in a well ordered fashion—at least locally—with adjacent N-containing and O-containing chains, the difference in electronic behavior results in a spatial separation of the VB and CB, which appear to be located on the two chain types, respectively (Figure 5a). Such spatial separation might possibly arise from a change in the electrostatic potential of the O-containing cells due to the presence of polar covalent bonds, as shown in previous literature,^[57,58] although our modeling could not find solid evidence due to the complexity of the problem and the polymeric nature of the system. However, this finding is in good agreement with experiment, as it relates the increase in performance up to FAT-1.0 to an increase in charge separation, as photoexcited electrons are gathering on O-containing chains and holes on N-containing ones, therefore slowing down the charge recombination and improving the performance. However, little control can be achieved in how the oxygen is arranged, and a more uniform distribution of oxygen among the chains improves the charge separation only marginally with respect to pristine $\text{g-C}_3\text{N}_4$ (Figure 5b,c).

It is therefore reasonable to propose that the performance trend as the amount of formic acid in the precursor increases depends on the local distribution as well as on the amount of oxygen introduced in the $\text{g-C}_3\text{N}_4$ chains: while a reasonable

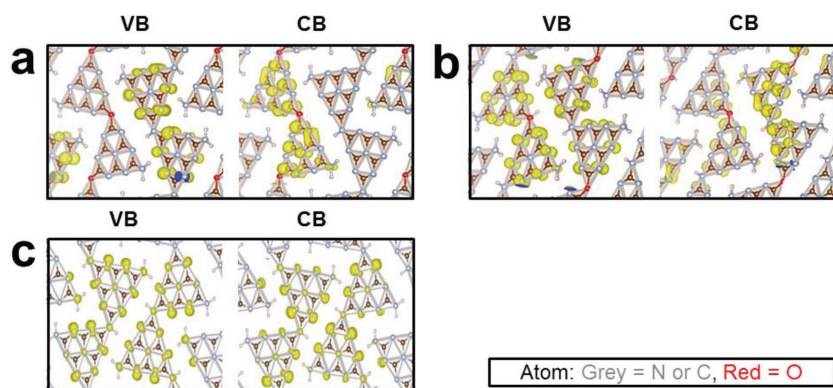


Figure 5. The highest occupied molecular orbitals (VB, left) and lowest unoccupied molecular orbitals (CB, right) (gray: N or C atoms, red: O atoms and yellow: orbitals) of a) highly ordered structure with O linkers and N linkers separately placed in different chains and b) disordered structure with O linkers and N linkers randomly placed in all chains. c) shows the VB and CB of non-doped $g\text{-C}_3\text{N}_4$, showing no spatial separation.

amount of formic acid will benefit the performances of the polymer by reducing the bandgap and, in some areas of the polymer, create a spatial separation between the VB and the CB that improves the e^-h^+ lifetime, a concentration of O-linkers and OH terminals that is too high would lower the probability of achieving this separation, leading to the decreased performances of FAT-1.5 and FAT-2.0. Therefore, a peak in performance is to be expected, as the control of the arrangement of oxygen within the framework is very difficult.

3. Conclusion

In summary, a novel strategy has been successfully developed to synthesize bandgap tunable, highly efficient, and robust organic semiconductor photocatalysts with enlarged optical window and suppressed charge recombination, thus addressing the two major challenges in photocatalysis. By controlling the polymerization process, the framework and electronic structure could be carefully tailored via incorporation of oxygen and nitrogen linkers as well as terminals between heptazine units. Moreover, the optimum FAT-1.0 sample exhibits 18 times higher H_2 evolution activity than reference $g\text{-C}_3\text{N}_4$ under visible light, resulting in high AQY of 8.3% and 2.5% at 420 and 500 nm. Surprisingly, it achieves 19 fold enhancement in O_2 evolution and exhibits AQY of 4.3% and about 1.0% at 420 and 500 nm. The excellent performance and band structure flexibility make the FAT polymers a group of promising semiconductors for potential applications including the construction of Z-scheme water splitting and photoelectrodes. Experimental and theoretical results have rationalized the observations in terms of narrowed bandgaps and enhanced charge separation, which are due to the oxygen incorporation into the linker/terminal position and reasonably higher amount of oxygen, narrower bandgap, leading to higher activity. Further increasing the oxygen content will result into bandgap increase. These findings pave a new approach to modifying the properties of polymers for efficient solar energy conversion through careful control of the polymerization process.

4. Experimental Section

Materials Preparation: In a typical formic acid treated polymer (denote FAT polymer) synthesis, 2 g (23.8 mmol) dicyandiamide (DCDA) (Fisher Scientific Ltd.) was first dissolved in 40 mL deionized (DI) water under strong agitation at 25 °C. Then a certain amount of formic acid (Sigma-Aldrich) (e.g., stoichiometry ratio of 0, 0.1, 0.2, 0.5, 0.8, 1.0, 1.5, and 2.0 formic acid to DCDA) was added into the DCDA solution and the solution was kept at 130 °C for 6 h before drying overnight under violent stirring. The resultant white crystalline precursor was transferred into a lidded high-quality alumina crucible, then placed inside a muffle furnace and heated at a ramp rate of 2 °C min^{-1} , and finally held at 550 °C for 4 h unless otherwise noted. The products were denoted as FAT-0, FAT-0.1, FAT-0.2, FAT-0.5, FAT-0.8, FAT-1.0, FAT-1.5, and FAT-2.0 with respect to the amount of formic acid used. FAT-0 is typical DCDA-derived $g\text{-C}_3\text{N}_4$. DI water, 0.1 M NaOH (Sigma-Aldrich) and HCl (Sigma-Aldrich) were used to wash the

produced powders adequately to remove all unreacted and potentially detrimental surface species. The FAT-based electrodes were prepared as below: 50 mg FAT polymer powder was added into a solution composed of 742.5 μL H_2O , 247.5 μL 2-propanol (Fisher Scientific Ltd.) and 10 μL Nafion (Fisher Scientific Ltd.) and the mixture was sonicated for 15 min. 100 μL of the resultant suspension was slowly dropped on an FTO glass. After drying under ambient conditions at 70 °C, it was calcined at 400 °C for 1 h in a muffle furnace.

Material Characterization: Powder x-ray diffraction (PXRD) measurements were taken using a StadiP diffractometer from Stoe company, a voltage of 40 kV, at 30 mA, using a Cu source with $K_{\alpha 1} = 1.540562$ Å and $K_{\alpha 2} = 1.544398$ Å. (Company: Stoe. Diffractometer: StadiP. Cu X-ray tube run at 40 kV 30 mA Capillary transmission geometry. Presample Ge (111) monochromator selects K alpha 1 only. Sample rotated in the beam. Dectris "Mythen 1k" silicon strip detector covering 18° 2 θ .) Diffuse reflectance spectra were obtained on a Shimadzu UV-Vis 2550 spectrophotometer fitted with an integrating sphere. A standard barium sulfate powder was used as a reference. Absorption spectra were calculated from the reflection measurements via the Kubelka-Munk transformation. ATR-FTIR spectroscopy was collected using a Perkin-Elmer 1605 FT-IR spectrometer in the wavenumber range 500–4000 cm^{-1} with a resolution of 0.5 cm^{-1} . Raman spectroscopic measurements were performed on a Renishaw InVia Raman Microscope, using a 325 nm excitation laser and a wavenumber range 100–2000 cm^{-1} . Scanning electron microscopy (SEM) images were gained from a JEOL JSM-7401F high-resolution Field Emission SEM operating at 2–3 kV. Due to the low conductivity of the semiconductor materials, an Au coating was sputtered onto the samples to improve the image quality. Specific surface area measurements were taken using the BET method (N_2 absorption, TriStar 3000, Micromeritics). XPS measurements were obtained on a ThermoScientific XPS K-alpha surface analysis machine using an Al source. The results of etched samples were carried out on the same XPS equipment. The XPS analysis was performed using CasaXPS software.

Photocatalytic Analysis: The photodeposition of cocatalysts on photocatalysts was carried out prior to each photocatalytic analysis. A certain amount of photocatalysts with 3 wt% cocatalysts (photodeposited using H_2PtCl_6 precursor) was dispersed in aqueous solution with proper electron acceptor (NaIO_3) or donor (TEOA) in a 130 mL reactor. Then the reactor was sealed, purged with Argon gas for 30 min, and then irradiated using a 300 W Xenon light source (Newport 66485-300XF-R1). During the photodeposition, periodic measurements were taken to determine if hydrogen or oxygen was produced at a stable rate to make sure the photodeposition occurred properly. The light intensity under working conditions is adjusted to ≈ 100 mW cm^{-2}

with a 420 nm long pass and a 710 nm short pass filter (420 nm < λ < 710 nm) which removes the IR to avoid thermal heating effect. In a typical H₂ evolution reaction, 50 mg of photocatalyst with 3 wt% of Pt cocatalyst was well dispersed in a 50 mL aqueous solution containing 10 vol% TEOA as electron donor inside a 130 mL top-irradiated reactor. In a typical O₂ evolution reaction, 20 mg of photocatalyst with 3 wt% of PtO_x cocatalyst was well dispersed in a 5 × 10⁻³ M NaIO₃ aqueous solution as electron acceptor inside a 130 mL top-irradiated reactor. These reaction conditions have been optimized including the amount of powder photocatalysts, cocatalysts, and solution. For the quantum yield measurement, 100 mg FAT-1.0 powder was used. The final results used the average activities calculated from five runs. Apparent quantum yield (AQY) (Φ) was calculated by using the following formula

$$\text{AQY}(\text{H}_2) = \frac{(2 \times \text{the number of evolved hydrogen molecules})}{(\text{the number of incident photons})} \times 100\%$$

$$\text{AQY}(\text{O}_2) = \frac{(4 \times \text{the number of evolved oxygen molecules})}{(\text{the number of incident photons})} \times 100\%$$

The light intensity measurements were taken by an optical power meter (Newport 1918-R) with an appropriate band pass filter (420, 500, 600, 700, 800 nm, $\lambda \pm 10$ nm at 10% of peak height, Comar Optics) inserted between a 300 W Xe light source (Newport 66485-300XF-R1) and reactor.

Computational Methodology: All calculations have been performed within the DFT framework as implemented in the VASP (Vienna Ab-initio Software Package) code.^[59] The electronic energy was obtained using PAW (projected augmented wave) potentials^[60] and plane-wave basis set, respectively, for core and valence electrons, using the Perdew–Burke–Ernzerhof (PBE) functional.^[61] Corrections were added to account for long-range interactions by semiempirical Grimme D3 dispersion method^[62] and for nonspherical contributions to the PAW potentials as natively built in the code. All energies are converged within a cutoff of 520 eV and an electronic self-consistent field (SCF) threshold of 10⁻⁵ eV. Convergence was determined using the tetrahedron method, implementing Blochl corrected smearing^[63] and in all cases spin polarization was disabled. The reciprocal lattice matrix was generated using a 5 × 5 × 5 K-points grid, using the Monkhorst-Pack method. The minimum energy structures were found using a built-in DIIS algorithm with a convergence force threshold of 10⁻³ eV Å⁻¹.

The bandgap for the nondoped system of is calculated as 1.01 eV, which underestimated the experimental value. Such results are to be expected when using a GGA level of theory such as the one employed by the PBE functional^[54] and are consistent with previous literature.^[55] Our analysis does not therefore make use of band structure but focuses on the charge distribution, which is expected to be reliable at this level of theory.

The unit cell for g-C₃N₄ was derived from previous literature^[64] through the Inorganic Crystal Structure Database. Each unit cell is organized in two planar layers accounting for a total of four linear organic chains, each composed of 2 tri-s-triazine units, 2 linker groups, and 2 terminal groups. In the g-C₃N₄ (FAT-0) model, all 16 groups contain nitrogen, being modeled as –NH– for linkers and –NH₂ for terminals. In the oxygen-doped (FAT) models, four such groups are modified to introduce oxygen, replacing the previous linker and terminal groups with –O– and –OH, respectively. In each of the different FAT models different groups are modified, in order to highlight the effect of local oxygen arrangement on the electronic properties of the material.

The definition of formation energy contributes to our understanding the energy change between graphitic carbon nitride and its O-modified homologues: being a difference between the energy of the cell and that of its components, it is largely influenced by the stability of the reference systems. In particular, the N₂ bond is much stronger than the C–N bond in the polymer, resulting in positive formation energy for g-C₃N₄. On the contrary, the C–O–C and C–O–H bonds in the FAT models appear

to correspond to a deeper energy well than the O₂ reference molecule, balancing the effect of N and giving a slightly negative (up to –0.11 eV per atom) formation energy to the FAT models. Ultimately, the formation energy is not a measure of the stability of the polymers relative to each other, but a measure relative to the elemental components of a system. However, it is the only way to compare the stabilities of unit cells comprising different numbers of atoms and gives a sensible reference point for the relative stabilities of the FAT polymers, which are shown to be very similar due to the identical bonds they are comprised of, but still dependent on the O substitution due to interchain H-bonds.

The formation energy for each unit cell has been calculated as the difference between the energy of the supercell and the energy of the compound elements divided by the number of atoms, via the formula

$$\Delta_f E = \frac{E_{\text{polymer}} - \sum E_i n_i}{N}$$

in which E_{polymer} is the energy of the polymer supercell, E_i and n_i represent, respectively, the energy of an atom of each element present in the polymer in its elemental state and the number of atoms of that element in the supercell, and N is the total number of atoms in the supercell, 144 for g-C₃N₄ and 140 for all FAT models. The elemental states considered are graphite for C and their respective diatomic molecules in vacuum for H, N, and O. Their energies have been calculated within suitable unit cells using the same parameters as described above for the polymers supercells.

Supporting Information

Supporting Information is available from the Wiley Online Library or from the author.

Acknowledgements

Y.W., Q.R., and Y.L. thank the CSC for Ph.D. funding. M.K.B and J.T. thank the Leverhulme Trust (RPG-2012-582). R.C. and J.T. acknowledge financial support from EPSRC (EP/N009533/1). J.T. thanks the Leverhulme Trust (RPG-2017-122) and Royal Society-Newton Advanced Fellowship grants (NA170422). F.S. thanks Cardiff University School of Chemistry for a fully funded PhD scholarship. Computing facilities for this work were provided by ARCCA at Cardiff University, HPC Wales, and through our membership of the UK's Materials Chemistry Consortium (MCC). The MCC is funded by EPSRC (EP/F067496). The authors are grateful to Dr. Matthew Quesne and Dr. Alberto Roldan for helpful advice and discussions.

Conflict of Interest

The authors declare no conflict of interest.

Keywords

bandgap, organic semiconductors, photocatalytic, polymers, water splitting

Received: April 9, 2018

Revised: May 15, 2018

Published online: June 28, 2018

[1] A. Kudo, Y. Miseki, *Chem. Soc. Rev.* **2009**, *38*, 253.

[2] G. Hess, *Chem. Eng. News* **2005**, *83*, 12.

- [3] R. T. Ross, T. L. Hsiao, *J. Appl. Phys.* **1977**, *48*, 4783.
- [4] J. R. Bolton, S. J. Strickler, J. S. Connolly, *Nature* **1985**, *316*, 495.
- [5] M. C. Hanna, A. J. Nozik, *J. Appl. Phys.* **2006**, *100*, 074510.
- [6] S. Hu, C. Xiang, S. Haussener, A. D. Berger, N. S. Lewis, *Energy Environ. Sci.* **2013**, *6*, 2984.
- [7] H. Doscher, J. F. Geisz, T. G. Deutsch, J. A. Turner, *Energy Environ. Sci.* **2014**, *7*, 2951.
- [8] Y. Wang, H. Suzuki, J. Xie, O. Tomita, D. J. Martin, M. Higashi, D. Kong, R. Abe, J. Tang, *Chem. Rev.* **2018**, *118*, 5201.
- [9] R. Konta, T. Ishii, H. Kato, A. Kudo, *J. Phys. Chem. B* **2004**, *108*, 8992.
- [10] K. Maeda, K. Teramura, D. Lu, T. Takata, N. Saito, Y. Inoue, K. Domen, *Nature* **2006**, *440*, 295.
- [11] X. Wang, K. Maeda, A. Thomas, K. Takanabe, G. Xin, J. M. Carlsson, K. Domen, M. Antonietti, *Nat. Mater.* **2009**, *8*, 76.
- [12] K. Kailasam, J. Schmidt, H. Bildirir, G. Zhang, S. Blechert, X. Wang, A. Thomas, *Macromol. Rapid Commun.* **2013**, *34*, 1008.
- [13] R. S. Sprick, J.-X. Jiang, B. Bonillo, S. Ren, T. Ratvijitvech, P. Guiglion, M. A. Zwijnenburg, D. J. Adams, A. I. Cooper, *J. Am. Chem. Soc.* **2015**, *137*, 3265.
- [14] V. S. Vyas, F. Haase, L. Stegbauer, G. Savasci, F. Podjaski, C. Ochsenfeld, B. V. Lotsch, *Nat. Commun.* **2015**, *6*, 8508.
- [15] L. Wang, Y. Wan, Y. Ding, S. Wu, Y. Zhang, X. Zhang, G. Zhang, Y. Xiong, X. Wu, J. Yang, H. Xu, *Adv. Mater.* **2017**, *29*, 1702428.
- [16] P. Pachfule, A. Acharjya, J. Roeser, T. Langenhahn, M. Schwarze, R. Schomäcker, A. Thomas, J. Schmidt, *J. Am. Chem. Soc.* **2018**, *140*, 1423.
- [17] J. Xie, S. A. Shevlin, Q. Ruan, S. J. A. Moniz, Y. Liu, X. Liu, Y. Li, C. C. Lau, Z. X. Guo, J. Tang, *Energy Environ. Sci.* **2018**.
- [18] D. J. Martin, K. Qiu, S. A. Shevlin, A. D. Handoko, X. Chen, Z. Guo, J. Tang, *Angew. Chem., Int. Ed.* **2014**, *53*, 9240.
- [19] J. Zhang, X. Wang, *Angew. Chem., Int. Ed.* **2015**, *54*, 7230.
- [20] J. Zhang, X. Chen, K. Takanabe, K. Maeda, K. Domen, J. D. Epping, X. Fu, M. Antonietti, X. Wang, *Angew. Chem., Int. Ed.* **2010**, *49*, 441.
- [21] S. Guo, Z. Deng, M. Li, B. Jiang, C. Tian, Q. Pan, H. Fu, *Angew. Chem., Int. Ed.* **2016**, *55*, 1830.
- [22] H. Yu, R. Shi, Y. Zhao, T. Bian, Y. Zhao, C. Zhou, G. I. N. Waterhouse, L.-Z. Wu, C.-H. Tung, T. Zhang, *Adv. Mater.* **2017**, *29*, 1605148.
- [23] M. Deifallah, P. F. McMillan, F. Corà, *J. Phys. Chem. C* **2008**, *112*, 5447.
- [24] A. B. Jorge, D. J. Martin, M. T. S. Dhanoa, A. S. Rahman, N. Makwana, J. Tang, A. Sella, F. Corà, S. Firth, J. A. Darr, P. F. McMillan, *J. Phys. Chem. C* **2013**, *117*, 7178.
- [25] G. Zhang, G. Li, Z.-A. Lan, L. Lin, A. Savateev, T. Heil, S. Zafeiratos, X. Wang, M. Antonietti, *Angew. Chem., Int. Ed.* **2017**, *56*, 13445.
- [26] Y. Chen, B. Wang, S. Lin, Y. Zhang, X. Wang, *J. Phys. Chem. C* **2014**, *118*, 29981.
- [27] Y. Wang, M. K. Bayazit, S. J. A. Moniz, Q. Ruan, C. C. Lau, N. Martsinovich, J. Tang, *Energy Environ. Sci.* **2017**, *10*, 1643.
- [28] K. Kailasam, M. B. Mesch, L. Möhlmann, M. Baar, S. Blechert, M. Schwarze, M. Schröder, R. Schomäcker, J. Senker, A. Thomas, *Energy Technol.* **2016**, *4*, 744.
- [29] A. Y. Deshmukh, D. B. Rathod, D. T. Tayade, R. A. Bhagwatkar, S. U. Patil, *Asian J. Chem.* **2010**, *22*, 8252.
- [30] Y. Zhang, J. Liu, G. Wu, W. Chen, *Nanoscale* **2012**, *4*, 5300.
- [31] Y. Hu, Y. Shim, J. Oh, S. Park, S. Park, Y. Ishii, *Chem. Mater.* **2017**, *29*, 5080.
- [32] A. Pfizmann, E. Fliedner, M. Fedtke, *Polym. Bull.* **1994**, *32*, 311.
- [33] N. E. A. El-Gamel, L. Seyfarth, J. Wagler, H. Ehrenberg, M. Schwarz, J. Senker, E. Kroke, *Chem.-Eur. J.* **2007**, *13*, 1158.
- [34] B. V. Lotsch, M. Döblinger, J. Sehnert, L. Seyfarth, J. Senker, O. Oeckler, W. Schnick, *Chem.-Eur. J.* **2007**, *13*, 4969.
- [35] Z. Zhou, J. Wang, J. Yu, Y. Shen, Y. Li, A. Liu, S. Liu, Y. Zhang, *J. Am. Chem. Soc.* **2015**, *137*, 2179.
- [36] A. C. Ferrari, S. E. Rodil, J. Robertson, *Phys. Rev. B* **2003**, *67*, 155306.
- [37] P. J. Larkin, M. P. Makowski, N. B. Colthup, *Spectrochim. Acta, Part A* **1999**, *55*, 1011.
- [38] R. O. Carter III, R. A. Dickie, J. W. Holubka, N. E. Lindsay, *Ind. Eng. Chem. Res.* **1989**, *28*, 48.
- [39] J. Oh, J.-H. Lee, J. C. Koo, H. R. Choi, Y. Lee, T. Kim, N. D. Luong, J.-D. Nam, *J. Mater. Chem.* **2010**, *20*, 9200.
- [40] D. Banfi, L. Patiny, *CHIMIA Int. J. Chem.* **2008**, *62*, 280.
- [41] C. Steinbeck, S. Krause, S. Kuhn, *J. Chem. Inf. Comput. Sci.* **2003**, *43*, 1733.
- [42] A. M. Castillo, L. Patiny, J. Wist, *J. Magn. Reson.* **2011**, *209*, 123.
- [43] Y. J. Oh, J. J. Yoo, Y. I. Kim, J. K. Yoon, H. N. Yoon, J.-H. Kim, S. B. Park, *Electrochim. Acta.* **2014**, *116*, 118.
- [44] C. Clayton, Y. Lu, *J. Electrochem. Soc.* **1986**, *133*, 2465.
- [45] J. Li, B. Shen, Z. Hong, B. Lin, B. Gao, Y. Chen, *Chem. Commun.* **2012**, *48*, 12017.
- [46] H. S. Casalongue, S. Kaya, V. Viswanathan, D. J. Miller, D. Friebe, H. A. Hansen, J. K. Nørskov, A. Nilsson, H. Ogasawara, *Nat. Commun.* **2013**, *4*, 2817.
- [47] D. Briggs, G. Beamson, *Anal. Chem.* **1993**, *65*, 1517.
- [48] P. Niu, L. Zhang, G. Liu, H.-M. Cheng, *Adv. Funct. Mater.* **2012**, *22*, 4763.
- [49] S. Yang, Y. Gong, J. Zhang, L. Zhan, L. Ma, Z. Fang, R. Vajtai, X. Wang, P. M. Ajayan, *Adv. Mater.* **2013**, *25*, 2452.
- [50] H. C. Schniepp, J.-L. Li, M. J. McAllister, H. Sai, M. Herrera-Alonso, D. H. Adamson, R. K. Prud'homme, R. Car, D. A. Saviile, I. A. Aksay, *J. Phys. Chem. B* **2006**, *110*, 8535.
- [51] M. Li, Y. Wang, P. Tang, N. Xie, Y. Zhao, X. Liu, G. Hu, J. Xie, Y. Zhao, J. Tang, T. Zhang, D. Ma, *Chem. Mater.* **2017**, *29*, 2769.
- [52] G. Zhang, J. Zhang, M. Zhang, X. Wang, *J. Mater. Chem.* **2012**, *22*, 8083.
- [53] J. Zhang, M. Grzelczak, Y. Hou, K. Maeda, K. Domen, X. Fu, M. Antonietti, X. Wang, *Chem. Sci.* **2012**, *3*, 443.
- [54] Q. Ruan, W. Luo, J. Xie, Y. Wang, X. Liu, Z. Bai, C. J. Carmalt, J. Tang, *Angew. Chem., Int. Ed.* **2017**, *56*, 8221.
- [55] Z. Gan, Y. Shan, J. Chen, Q. Gui, Q. Zhang, S. Nie, X. Wu, *Nano Res.* **2016**, *9*, 1801.
- [56] R. Godin, Y. Wang, M. A. Zwijnenburg, J. Tang, J. R. Durrant, *J. Am. Chem. Soc.* **2017**, *139*, 5216.
- [57] W. Hu, L. Lin, C. Yang, J. Dai, J. Yang, *Nano Lett.* **2016**, *16*, 1675.
- [58] W. Hu, L. Lin, R. Zhang, C. Yang, J. Yang, *J. Am. Chem. Soc.* **2017**, *139*, 15429.
- [59] G. Kresse, J. Furthmüller, *Comp. Mater. Sci.* **1996**, *6*, 15.
- [60] P. E. Blöchl, *Phys. Rev. B* **1994**, *50*, 17953.
- [61] J. P. Perdew, K. Burke, M. Ernzerhof, *Phys. Rev. Lett.* **1996**, *77*, 3865.
- [62] S. Grimme, J. Antony, S. Ehrlich, H. Krieg, *J. Chem. Phys.* **2010**, *132*, 154104.
- [63] P. E. Blöchl, O. Jepsen, O. K. Andersen, *Phys. Rev. B* **1994**, *49*, 16223.
- [64] F. Fina, S. K. Callear, G. M. Carins, J. T. S. Irvine, *Chem. Mater.* **2015**, *27*, 2612.